Effect of gas atmosphere on catalytic behaviour of zirconia, ceria and ceria-zirconia catalysts in valeric acid ketonization

Yu. A. Zaitseva, V. N. Panchenko, M. N. Simonov, A. A. Shutilov, G. N. Zenkovets, M. Renz, I. L. Simakova,V. N. Parmon

Boreskov Institute of Catalysis, Lavrentieva 5, 630090 Novosibirsk, Russian Federation

e-mail: simakova@catalysis.ru

tel. +7 383 3269531

fax +7 383 3308056

Abstract

Ketonization of valeric acid, which can be obtained by lignocellulosic biomass conversion, was carried out in a fixed bed flow reactor over ZrO_2, 5-20%CeO_2/ZrO_2 and CeO_2 both under hydrogen and nitrogen stream at 628K and atmospheric pressure. Regardless gas-carrier 10 wt.% CeO_2/ZrO_2 was found to show higher catalytic activity compared to zirconia per se as well as other ceria modified zirconia while ceria per se exhibited very low catalytic activity. All catalysts provided higher acid conversion in H_2 than in N_2 whereas selectivity to 5-nonanone was insensitive to gas atmosphere. XRD, FTIR, UV-Vis DRS, XPS, HRTEM methods were applied to characterize catalysts in reduced and unreduced states simulating corresponding reaction conditions during acid ketonization. XRD did not reveal any changes in zirconia and ceria/zirconia lattice parameters as well as crystalline phase depending on gas atmosphere while insertion of ceria in zirconia caused notable increase in lattice parameter indicating some distortion of crystalline structure. According to XPS, FTIR and UV-Vis methods, the carrier gas was found to affect catalyst surface composition leading to alteration in Lewis acid sites ratio. Appearance of Zr^{3+} cations was observed on the ZrO_2 surface after hydrogen pretreatment whereas only Zr^{4+} cations were determined using nitrogen as a gas-carrier. These changes of catalyst's surface cation composition affected corresponding activity in ketonization probably being crucial for reaction mechanism involving metal cations catalytic centers for acid adsorption and COO^- stabilization at the initial step.

Keywords: ceria, zirconia, ketonization, effect of gas atmosphere, valeric acid, biomass processing

Introduction

Currently the development of supplementary methods for obtaining motor fuels and valuable chemicals by biomass processing is a promising way for sustainable development of global chemical industry. In general, lignocellulosic feedstocks are considered as a preferred source for energy and chemical production because it is non-edible and the most abundant class of biomass [1]. Organic acids, the largest group of the promising biomass derivatives, can be produced by fermentation and/or chemical transformation of glucose obtained by biomass hydrolysis. For example, valeric acid is a product of levulinic acid conversion, one of the platform molecules produced by dehydration of glucose [1,2]. Carboxylic acids can be converted into ketones accompanied by carbon dioxide and water release via catalytic decarboxylation of two acid molecules in the presence of metal oxides. This process is considered to be environmentally friendly because non-polluting by-products are formed. Ketones are useful products and find wide applications as solvents, as well as in ink manufacturing [3], corrosion inhibition [4], personal care products [5], and dishwashing detergents [6]. At the same time ketones are reported to be used as key precursors for producing fuel components via their consecutive reduction into alkanes. One-pot mode of carboxylic acid decarboxylation coupling followed by ketone hydrogenation into alkane over Pt(Pd)/M_xO_y bifunctional catalyst can be considered as a more attractive way to produce green diesel components probably providing higher selectivity due to immediate hydrogenation of adsorbed intermediate products coming from ketonization (Fig. 1). Although acid decarboxylation usually does not require reducing atmosphere and typically is carried out in inert gas, consideration of ketonization as a part of one-pot technology requires to optimize the process and to study catalytic behavior of metal oxides in acid ketonization under hydrogen gas atmosphere in comparison to nitrogen as well as to investigate the influence of gas atmosphere on the state of the catalyst active component.

Ketonization of various carboxylic acids on different metal oxides has been studied extensively, although the most suitable one was not identified. Previous reports were mainly focused on the ketonization of aliphatic acids [7-9], oxy-acids [2,10,11], fatty acids [4,8,9,12-19] acids and dibasic acids [20-22] to form symmetric, non-symmetric, fatty and cyclic ketones over catalysts based on MgO

[13,19], Nb_2O_5[2,10,11], CeO_2[7,10,23-26], MnO_2[7,27,28], TiO_2[7,29-31], SiO_2[7,26], Al_2O_3[7,12,26], ZrO_2[9,10,15,26,32,33], Cr_2O_3[34,35], Fe_3O_4[36,37], $Ba(OH)_2$ [20-22], NaOH [38], $FeSO_4$ [20] at 558-723K, ambient pressure and inert atmosphere. Nevertheless there are scarce publications concerning influence of gas flow composition on the oxide catalyst reactivity. Thus Taimoor et al. have reported a beneficial effect of hydrogen on acetic acid conversion in decarboxylating coupling compared with nitrogen and carbon dioxide atmosphere [39] but possible reasons for such changes in catalytic activity were not elucidated.

In the present work we have studied catalytic activity of mono metal oxides ZrO_2, CeO_2, and bimetallic oxides CeO_2/ZrO_2 with varied CeO_2 loading in valeric acid ketonization carried out in hydrogen and nitrogen atmosphere. HRTEM, XRD, FTIR *in situ*, UV-Vis *in situ*, XPS *ex-situ*, and low temperature N_2 physisorption techniques were applied to identify structural and electronic changes in the state of the oxides being exposed to the corresponding gas-carrier that could be responsible for catalytic activity.

Experimental

Materials

Valeric acid (99%) and 5-nonanone (98%) was purchased from Acros Organics. The acid was degassed by argon and used as reagent. Both acid and ketone were used as standards for gas chromatographic analysis. H_2 was purified from oxygen by passing through nickel chromium catalyst.

Catalyst preparation

ZrO_2 and CeO_2 catalysts were prepared by precipitation from water solutions of $Zr(NO_3)_4$ (pH=7) and $Ce(NO_3)_3$ (pH=8) with 12.5(wt.%) NH_4OH aqueous solution. Thereafter the precipitate was filtrated, washed with water, dried in the dry box at 383K and calcined at 723K in muffle furnace for 4 h. $Zr(NO_3)_4$ and $Ce(NO_3)_3$ aqueous solutions were obtained from $Zr(NO_3)_4 \times 4H_2O$(Aldrich) and $Ce(NO_3)_3 \times 6H_2O$(Aldrich).

10%(wt.%)CeO_2/ZrO_2 was prepared by incipient wetness impregnation of the ZrO_2 support with $Ce(NO_3)_3$ aqueous solution. The catalyst was dried at 383K for

10 h and then calcined in muffle furnace at 773K for 4 h. The $Ce(NO_3)_3$ aqueous solution was prepared from $Ce(NO_3)_3 \times 6H_2O$ (Aldrich).

Catalytic reaction

The ketonization was carried out in a fixed bed flow reactor in the gas phase at 628K under hydrogen or nitrogen stream at ~1 bar with the flow rate of 30 cm^3/min. Before the reaction the catalyst (m=0.5g, fraction=0.25÷0.5mm) was mixed with quartz (m=3g, fraction=1.0÷1.25mm) and heated in hydrogen stream until reaction temperature. Neat valeric acid was then fed using a syringe pump with liquid hourly space velocity (LHSV) = 0,34 $cm^3/(g \cdot h)$. Catalyst was kept in the reagent flow at reaction temperature for 1 hour, and then condensable products were collected in the trap with liquid nitrogen through 2 hours.

Analysis and measurements

X-ray diffraction (XRD) analysis was performed on a D8 ("Bruker") diffractometer with CuK_α radiation. The intensity data were collected over 2θ range of 15–90° with a 0.05° step size and using a counting time of 5 s per point. Phase identification was carried out by comparison with JCPDF database cards. The lattice parameters of monoclinic ZrO_2 were determined using (001), (110), (111), (200) patterns by Rietveld method. The lattice parameter of tetragonal ZrO_2 was determined using (111) pattern by "POLYCRYSTAL" program. The CSD was determined by Scherrer equation using (111) pattern half-width.

X-ray photoelectron spectroscopy (XPS) was performed *ex-situ* on a SPECS ("SPECS GmbH") spectrometer by using AlK_α (1486.6 eV) radiation as the excitation source and pass energy of 20eV. The binding energies were calibrated using ground levels $Au4f_{7/2}$ (84.0 eV) and $Cu2p_{3/2}$ (932.7 eV). Charging of specimen surface was corrected by internal standard method Zr $3d_{5/2}$ (182.3 eV) in ZrO_2.Vacuum level during XPS analysis was $1*10^{-9}$ mbar.

High-resolution electron microscopy (HRTEM) was carried out with a JEM 2010 microscope with resolution of 0.14 nm at accelerating voltage 200 kV. The local elemental energy-dispersive X-ray (EDX) microanalysis was performed using an EDAX spectrometer.

UV-vis diffuse reflectance spectra were *in situ* recorded in the range of 190-900 nm and resolution of 2 nm using a UV-Shimadzu UV-vis spectrometer with IRS-

250A prefix diffuse reflection. $BaSO_4$ was used as standard. Samples of catalysts were placed, in form of dry powders, into a special cell for DR UV-vis measurements. All experiments were performed under vacuum or argon atmosphere using the "break-seal" technique.

The DRS spectra are presented according to the Kubelka–Munk function [40]:

$$F(R) = \frac{(1-R)^2}{2R} \qquad (1)$$

here *R* is reflection coefficient.

Infrared spectroscopy study of CO adsorption was recorded *in situ* in the range of 400-6000 cm^{-1} and resolution of 4 cm^{-1} on a FTIR-8300 Shimadzu spectrometer. The sample was pressed in form of tablets (mass typically 20–40 mg, p= 9–15 mg/cm^2). The tablet sample was heated at 723K for 1 h in air, and then was reduced by H_2 in a special *in situ* cell at the same temperature for 30 minutes. Thereafter hydrogen was pumped out for 30 minutes at 723K. The treatment was repeated 3 times. CO was adsorbed in small doses 0.02 Torr up to CO pressure 5 Torr at 110 K.

The specific surface of the samples was calculated by the BET method using an argon adsorption isotherm at 77K.

The reaction products were identified by Agilent Technologies 7000 GC/MS Triple Quad using fused silica column Agilent HP-5ms (30m/0.25mm/0.25µm) (USA).

The product content was analyzed by "Chromos 1000" GC equipped with a flame ionization detector (FID) and fused silica column Stabilwax-DA (50 m/0.32 mm/0.5µm) (USA) at 373-473K with temperature ramp 10K/min.

The conversion of valeric acid was defined as the molar percentage of the reacted acid to all liquid products using the following equation 2:

$$\alpha(\%) = \frac{C_a^0 - C_a}{C_a^0} \times 100 \qquad (2)$$

The selectivity to 5-nonanone was calculated as the weight percentage relatively to all organic liquid products, as shown in equation 3

$$S(\%) = \frac{2 \times C_k}{C_a^0 - C_a + \sum_k C_k} \times 100 \qquad (3)$$

, where C_a^o, C_a– are the concentrations (mol/l) of inlet fed valeric acid, unreacted valeric acid and ΣC_k – sum of concentrations (mol/l) of produced ketones 5-nonanone, respectively. According to the stoichiometry of the reaction two molecules of valeric acid consumed for every molecule of 5-nonanone or other ketone formed. Therefore concentration of 5-nonanone was mulitiplied by 2 in numenator and sum of concentrations of all ketones is added in denominator [41].

Results and discussion

XRD

The X-ray patterns of the samples are presented in Fig. 2. The ZrO_2 sample consisted of a mixture of monoclinic and tetragonal ZrO_2 phases. The reductive treatment of oxide with hydrogen resulted in a negligible increase of the monoclinic phase (Table 1). The values of lattice parameters and coherently scattering domain (D_{CSD}) for ZrO_2 were independent on the gas atmosphere.

The bimetallic oxide 10%CeO_2/ZrO_2 sample showed diffraction patterns of ZrO_2 in tetragonal phase with a minor admixture of monoclinic zirconia. Absence of CeO_2 phase denoted formation of the solid solution. The phase composition, lattice parameter and CSD of 10%CeO_2/ZrO_2 remained invariable after hydrogen treatment. Thus, no considerable effect of hydrogen treatment on phase composition and structure parameters of the samples 10%CeO_2/ZrO_2 and ZrO_2 at temperature up to 723K was observed.

A comparison of the XRD data for ZrO_2 and 10%CeO_2/ZrO_2 illustrated the increasing amount of tetragonal ZrO_2 phase and its lattice parameter when zirconia was modified by ceria. The observed structural change could be responsible for the tetragonal phase stabilization during ZrO_2 modification. The lattice parameter growth can be explained by the formation of solid solution. According to the literature data [42], substitution of some Zr^{4+} ions by Ce^{3+} or Ce^{4+} favors the ZrO_2 lattice distortion as cerium ion radius ($r(Ce^{3+})$=1.02 Å, $r(Ce^{4+})$=0.92 Å) is larger than zirconium one ($r(Zr^{4+})$=0.77 Å).

HRTEM and EDX

According to HRTEM, 10%CeO_2/ZrO_2 sample represented agglomerates with wide size distribution from 50 nm to 5 μm. Agglomerates were mainly composed of

highly ordered small crystallites of ZrO_2 tetragonal phase with size of 5.5-8 nm. At the same time some particles of size 13–15 nm were observed that consist of incoherently accreted smaller crystallites with formation of highly disoriented inter-grain boundaries between these crystallites (Fig.3). According to the EDX data, elemental composition in different domains slightly varied from 87.94 to 95.44% for zirconium and from 12.06 to 4.56% for cerium (Fig.4). However, individual phase of ceria was not observed. These results clearly showed uniform Ce component distribution in the zirconia sample.

XPS *ex situ*

XPS measurements (Fig. 5) of both ZrO_2 and 10%CeO_2/ZrO_2 unreduced samples showed binding energy values of Zr $3d_{5/2}$ (182.8 eV) and Zr $3d_{3/2}$ (184.4 eV) indicating the presence of Zr^{4+} ions [43]. The Ce 3d spectra consisted of two sets of spin-orbit multiplets featuring $3d_{3/2}$ and $3d_{5/2}$ (represented as u and v, respectively) contributions (Fig. 6) [44]. The peaks labeled v and v'' have been assigned to a mixing of Ce $3d^9$ $4f^2$ O $2p^4$ and Ce $3d^9$ $4f^1$ O $2p^5$ Ce(IV) final states, and the peak denoted v''' corresponded to Ce $3d^9$ $4f^0$ O $2p^6$ Ce(IV) final state. On the other hand, lines v_0 and v' were assigned to Ce $3d^9$ $4f^2$ O $2p^5$ and Ce $3d^9$ $4f^1$ O $2p^6$ of Ce(III). The same assignment could be applied to the u structures, which corresponded to the Ce $3d_{3/2}$ levels.

As can be seen from Fig. 7 (shown only for 10%CeO_2/ZrO_2) the O1s spectra obtained for the samples showed a broad peak in the domain of 527-535 eV including a peak at 530.3 eV and small additional peaks at 532.1 and 528.6 eV. The peak at 530.3 eV was assigned to nucleophilic surface lattice oxygen ions, while the small peak at 532.1 eV might be attributed to surface hydroxyls, the peak at 528.6 eV was applied to improve spectra approximation (its presence could be caused by induced charging of specimen surface during analysis).

The surface chemical compositions of ZrO_2 and 10%CeO_2/ZrO_2 samples were determined on the basis of the XPS *ex situ* data (Table 2). This method did not reveal presence of Zr^{3+} cations in both catalysts ZrO_2 and 10%CeO_2/ZrO_2 even after reduction in hydrogen. Unreduced ceria-modified zirconia sample showed the presence of both Ce^{3+} and Ce^{4+} cations and after hydrogen treatment Ce^{3+} surface concentration rose from 2.6 to 3.2% with a decrease of Ce^{4+} cation content from 1.7 to 1.4wt. %. Increase in the total cation concentration due to decreasing

of total oxygen content was observed after the reductive catalyst treatment for ZrO_2 from 28.4 to 30.1%, for 10%CeO_2/ZrO_2 from 31.3 to 32.4% as well as after modification of ZrO_2 by CeO_2 from 28.4 to 31.3% before reduction, and from 30.1 to 32.4% after reduction.

Since the presence of surface cations is of great importance for carboxylic acid decarboxylative coupling two independent different techniques UV-Vis DRS and DRIFT were additionally applied for *in situ* characterization of CeO_2, ZrO_2 and 10%CeO_2/ZrO_2 surface chemical composition.

UV-Vis DRS *in situ*

Figure 8 shows the UV-vis spectra of CeO_2, ZrO_2 and 10%CeO_2/ZrO_2 samples. The observed absorption maxima and their assignments are listed in Table 3.

Two absorption maxima centered at 226 and 265 nm were observed for ZrO_2 sample in its UV-vis spectrum. The both maxima corresponded to $O \rightarrow Zr^{4+}$ charge-transfer transitions [45, 46]. The intensity of the absorption at 265 nm decreased after hydrogen treatment that indicated the decrease of Zr^{4+} ion concentration and appearance of Zr^{3+} ions (Fig. 8 a).

CeO_2 spectrum represented a broad maximum centered at 300 nm covering three maxima at 250, 270 and 334 nm corresponded to $O \rightarrow Ce^{3+}$, $O \rightarrow Ce^{4+}$ charge-transfer transitions and interband transitions of CeO_2 (Ce^{n+} - O - Ce^{n+}, n=3, 4), respectively (Fig. 8 b) (maxima are not presented in Fig. 8 b). The decrease of adsorption intensity at 300 nm was observed in the case of hydrogen as carrier gas. In general, the change was associated with a decrease of Ce^{4+} ions due to their reduction into Ce^{3+}. In addition a wide maximum presented at 700 nm was assigned to interband transitions (Fig. 8 b).

The 10%CeO_2/ZrO_2 sample exhibited absorption at 300 nm, which contained five maxima at 250, 270, 306, 350 and 380 nm (Fig. 8 c) (maxima are not presented in Fig. 8 c). The former two absorption maxima were related to $O \rightarrow Ce^{3+}$ and $O \rightarrow Ce^{4+}$, $O \rightarrow Zr^{4+}$ charge-transfer transitions, respectively [46-51]. The latter three maxima were attributed to the interband transitions of CeO_2 (Ce^{n+} - O - Ce^{n+}, Ce^{n+} -O- Zr^{4+} n=3, 4). When using hydrogen as the carrier gas the decrease of absorption intensity at 270 nm was observed due to reducing a part of Ce^{4+} and Zr^{4+} ions to Ce^{3+} and Zr^{3+} ions, respectively. The wide maximum at 450

nm due to Ce^{n+}-O-Ce^{n+} and Ce^{n+} -O- Zr^{n+} (n=3, 4) interband transitions was detected under the same conditions.

Thus, based on the Zr^{3+} and Ce^{3+} ions formation, it can be concluded that the reduction of ZrO_2, CeO_2 and 10%CeO_2/ZrO_2 occurred during hydrogen treatment.

IRS *in situ*

In addition CO was used as a probe molecule to IR study of changes in acidity (amount and strength of Lewis sites) of the reduced samples compared to unreduced ones. In a spectrum of the reduced ZrO_2 sample bands corresponding to carbonyl complexes of Zr^{3+} (2075, 2100, 2153 cm^{-1}) and Zr^{4+} (2180, 2197 cm^{-1}) cations were observed (Fig. 9) [52]. The intensity of Zr^{3+}-O complexes was higher than Zr^{4+}-O intensity, indicating large extent of ZrO_2 surface reduction. CO adsorption on 10%CeO_2/ZrO_2 showed a broad band in range 2100-2250 cm^{-1}, which contained six bands corresponding to carbonyl complexes of Zr^{4+} and Ce^{4+} (2185, 2197 cm^{-1}), Ce^{4+} (2170 cm^{-1}), Ce^{4+} or Zr^{3+} (2156 cm^{-1}), Ce^{3+} or Zr^{4+} (2110, 2125 cm^{-1}) cations [52]. Thus, both IR and UV-Vis *in situ* spectroscopy studies indicate the presence of Zr^{3+} ions on the ZrO_2 surface and Ce^{3+} and Zr^{3+} ions on the 10%CeO_2/ZrO_2 surface after hydrogen treatment.

It should be noted that FTIR and UV-Vis spectroscopy data on the Zr^{3+} presence in reduced ZrO_2 and 10%CeO_2/ZrO_2 samples did not correspond to XPS performed *ex-situ* since FTIR and UV-Vis DRS analyses were carried out *in situ*. Therefore optical methods data concerning Zr^{3+} cations presence were used to explain catalytic behavior of the tested oxides.

Catalytic properties

Metal oxide catalysts CeO_2, ZrO_2, and CeO_2/ZrO_2 have been tested in the ketonization of valeric acid in both hydrogen and nitrogen atmosphere in comparable reaction conditions in the absence of mass transfer limitations. According to GC/MS analysis, the main product of the reaction is 5-nonanone, while major side products are carboxylic acids (formic, acetic, propionic, butyric), ketones (acetone, butanone-2, γ-valerolactone, δ-valerolactone, hexanone-2, heptanone-3, octanone-2) and aldehyde (pentanal) with concentrations of no more than 3%.

Among the tested metal oxides CeO_2 exhibited the lowest valeric acid conversion 40% in H_2 and 31% in N_2 while showed comparable selectivity to 5-nonanone of 76% and 80% in H_2 and N_2 respectively (Fig. 10). It is worth to note that CeO_2 sample with large particle size and low surface area was selected and applied in valeric acid ketonization to achieve as high catalytic activity as possible using ceria catalyst. Earlier it was reported in [23, 53] that ceria active sites for the acid ketonization are mainly formed on the CeO_2 (111) plane, which are located predominantly on large ceria particles indicating increase of catalytic activity with size growth of CeO_2 particles. Nevertheless CeO_2 that had surface area 25 m^2/g in our experiments demonstrated very low activity compared to other tested oxide catalysts.

The most interesting catalytic results were obtained over zirconia and CeO_2/ZrO_2 illustrating beneficial effect of ceria introduction regardless gas atmosphere. Zirconia was found to demonstrate much better catalytic performance than ceria showing valeric acid conversion 83% and 66% as well as selectivity to 5-nonanone 78% and 80% in H_2 and N_2, respectively. Introduction of inactive per se ceria into zirconia in small amounts from 5 to 20 wt.% affected surprisingly strongly valeric acid conversion showing the highest acid conversion at ceria content 10 wt.% while selectivity to 5-nonanone seemed to be insensitive to the amount of ceria introduced. Note that zirconia specific surface area decreased from 105 m^2/g to 79 m^2/g after introduction of ceria. Therefore changes of the catalytic activity could not be referred to the surface area. According to HRTEM, 10%CeO_2/ZrO_2 represents mainly ZrO_2 tetragonal phase particles with the size of 5.5-8 nm and some particles of the size 13–15 nm which consist of incoherently accreted smaller crystallites while no individual CeO_2 phase was detected by EDX. Formation of such distorted ceria- zirconia crystalline surface structures could contribute additionally to the catalytic activity of ceria modified zirconia. The reason is that such structures contain more moveable and thereby more reactive lattice oxygen which interacts more actively with the acids adsorbed on the oxide surface to form carboxylates followed by abstraction of α-proton from one carboxylate with formation of anion radical. The latter attacks another carboxylate to produce β-ketoacid followed by decarboxylation to form ketone [26]. Furthermore, additional effect of intergrain boundaries on catalytic activity can take place. Quite similar effect of increased catalytic activity was observed in alcohol dehydration over

Al_2O_3, due to Increasing the contact interface and formation of grain boundaries [54].

A very interesting gas-carrier effect was found for CeO_2, ZrO_2, and 10%CeO_2/ZrO_2. To investigate H_2 influence the process was carried out over the catalysts under either hydrogen or nitrogen. According to the results listed in Table 4 all catalysts showed higher acid conversion in hydrogen compared to nitrogen, whereas selectivity seemed to be unaffected by gas atmosphere. The XPS and optical investigations indicated that the surface features of the oxides mainly contributed to their catalytic performance in the ketonization of valeric acid. Thus the appearance of Zr^{3+} cations due to the replacement of N_2 by H_2 was accompanied by an increase of ZrO_2 activity, while there are only Zr^{4+} cations on the initial unreduced zirconia surface. The same regularities although less prominent were observed for ceria containing mixed oxides. There were Zr^{3+} and Ce^{3+} cations appeared after reduction of 10%CeO_2/ZrO_2 catalyst. But contrary to Zr^{3+} cations, identified only after the reduction, Ce^{3+} cations were already presented on the unreduced 10%CeO_2/ZrO_2 surface due to the formation of O-vacancies [55,56. Therefore, effect of hydrogen treatment on Ce containing catalysts could be prominent depending on the magnitude of changes in Ce^{3+} content during reduction. According to UV-Vis data hydrogen treatment of neat CeO_2 resulted in profound reduction of Ce(IV) that gave a rise to catalytic activity under the reductive conditions. According to XPS and optical data the reduction of samples resulted in a decrease of Lewis site acidity ($Ce^{4+}\rightarrow Ce^{3+}$, $Zr^{4+}\rightarrow Zr^{3+}$) and increased amount of Lewis acid sites. The catalytic activity change observed after reductive pretreatment indicates sensitivity of ketonization towards Lewis site acidity and its content. From the mechanistic viewpoint less oxide surface acidity probably benefits adsorption acidic reactants on the catalyst surface while evidently the main factor affecting the conversion of valeric acid into 5-nonanone is the delicate balance between Lewis acid and basic sites.

Conclusion

Ketonization of valeric acid, which can be derived from biomass, to 5-nonanone has been studied in both under hydrogen and nitrogen stream at 628K and atmospheric pressure. The process was shown to occur with high conversion and selectivity over ZrO_2 and (5-20%) CeO_2/ZrO_2 while CeO_2 exhibited very low

valeric acid conversion regardless gas atmosphere. Insertion of inactive ceria into zirconia leads to notable increase of valeric acid conversion. Using XRD and HRTEM data for 10%CeO_2/ZrO_2 the reasons for increasing catalytic activity suggested to be due to solid solution formation with uniform cerium distribution, higher Lewis site content and formation of highly defective surface. According to XPS, FTIR and UV-Vis methods, the carrier gas was found to affect catalyst surface chemical composition leading to alteration in catalytic properties. The valeric acid conversion over zirconia and ceria-zirconia catalysts was found to be significantly lower under nitrogen compared to that in hydrogen. It was concluded that valeric acid ketonization reaction rate depends on Lewis sites acidity which is dependent on reduction of the catalyst surface.

Acknowledgments

Financial support from the Russian Foundation of Basic Research (RFBR Grant No 11-03-94001-CSIC) is gratefully acknowledged. The authors also wish to thank Dr. Evgeniy Gerasimov, Dr. Igor Prosvirin, Dr. Demid Demidov from the Department of Physicochemical Methods at the Boreskov Institute of Catalysis for TEM and XPS measurements.

References

1. Alonso DM, Bond JQ, Dumesic JA (2010) Green Chem 12:1493-1513
2. Serrano-Ruiz JC, Wang D, Dumesic JA (2010) Green Chem 12:574–577
3. Malhotra SL, Wong RW, Breton MP (2002) Patent US 6461417
4. Westfechtel A, Breucker C, Gutsche B, Jeromin L, Eierdanz H, Baumann H, Schmid KH, Nonnenkamp W (1993) Patent DE 4121117
5. Seipel W, Hensen H, Boyxen N (2001) Patent DE 19958521
6. Tomlinson AD (2001) Patent WO 2001094522
7. Glinski M, Kijenski J, Jakubowski A (1995) Appl Catal A Gen 128:209-217
8. Glinski M, Kijenski J (2000) React Kinet Catal Lett 69:123-128
9. Parida K, Mishra HK (1999) J Mol Catal A Chem 139:73-80
10. Serrano-Ruiz JC, Dumesic JA (2009) Green Chem 11:1101–1104
11. Serrano-Ruiz JC, Dumesic JA (2009) ChemSusChem 2:581 – 586
12. Leung A, Boocock DGB, Konar SK (1995) Energy Fuels 9:913–920
13. Gaertner CA, Serrano-Ruiz JC, Braden DJ, Dumesic JA (2010) Ind Eng Chem Res 49:6027–6033
14. Saito N (1996) Patent JP 08198796

15. Yakerson VI, Rubinshtein AM, Gorskaya LA (1970) Patent GB 1208802
16. Graille J, Pioch D (1991) Patent EP 457665
17. Pioch D, Lescure R, Graille J (1995) Ol Corps Gras Lipides 2:386–389
18. Mueller-Erlwein E, Rosenberger B (1990) Chem Ing Tech 62:512–513
19. Corma A, Renz M, Schaverien C (2008) ChemSusChem 1:739 – 741
20. Bayer & Co (1911) Patent DE 256622
21. Vavon G, Apchie A (1928) Bull Soc Chim 43:667–677
22. Thorpe JF, Kon GAR (1941) Org Synth Coll 1:192–194
23. Nagashima O, Sato S, Takahashi R, Sodesawa T (2005) J Mol Catal A Chem 227:231-239
24. Klein-Homann W (1988) Patent DE 3709765
25. Stubenrauch J, Brisha E, Vohs JM (1996) Catal Today 28:431-441
26. Pulido A, Oliver-Tomas B, Renz M, Boronat M, and Corma A (2012) Ketonic decarboxylation reaction mechanism: A combined experimental and DFT study. ChemSusChem Doi:10.1002/cssc.201200419
27. Hendren TS, Dooley KM (2003) Catal Today 85:333-351
28. Novothy R, Paulsen S (1963) Patent DE 1158050
29. Kim KS, Barteau MA (1990) J Catal 125:353-375
30. Pestman R, Van Duijne A, Pieterse JAZ, Ponec V (1995) J Mol Catal A 103 :175-180
31. Martinez R, Huff MC, Barteau MA (2004) J Catal 222 :404-409
32. Matsuoka K, Tagawa K (1985) Patent JP 61207354
33. Daicel Chem Ind (1982) Patent JP 57197237
34. Kuriacose JC, Swaminathan R (1969) J Catal 14:348-354
35. Swaminathan R, Kuriacose JC (1970) J Catal 16:357-362
36. Cressely J, Farkhani D, Deluzarche A, Kiennemann A (1984) Mater Chem Phys 11:413-431
37. Kuriacose JC, Jewur SS (1977) J Catal 50:330-341
38. Renz M, Corma A (2004) Eur J Org Chem 2004:2036–2039
39. Taimoor AA, Favre-Reguillon A, Vanoye L, Pitault I (2012) Catal Sci Technol 2:359-363
40. Kustov LM (1997) Topics Catal 4:131-144
41. Emmanuel NM (1978) Uspekhi Khimii 8:1329-1396

42. Kaspar J, Fornasiero P (2002) In: Trovarelli A (ed) Catalysis by Ceria and Related Materials. Imperial College Press, London
43. Reddy DD, Chowdhury B, Smirniotis PG (2001) Appl Catal A Gen 211:19-30
44. Rango R, Kaspar G, Meriani S, di Monte R, Graziani M (1994) Catal Lett 24:107-112
45. Rao G, Sahu H (2001) Proc Indian Acad Sci (Chem Sci) 113:651–658
46. Navío JA, Hidalgo MC, Colón G, Botta SG, Litter MI (2001) Langmuir 17:202-210
47. Timofeeva MN, Jhung SH, Hwang YK, Kim DK, Panchenko VN, Melgunov MS, Chesalov YA, Chang JS (2007) Appl Catal A Gen 317:1-10
48. Kaneko H, Taku S, Tamaura Y (2011) Sol Energy 85:2321–2330
49. Maia TA, Assaf JM, Assaf EM (2012) Mater Chem Phys 132:1029-1034
50. Zhou HP, Si R, Song WG, Yan CH (2009) J Solid State Chem 182:2475–2485
51. Si R, Zhang YW, Li SJ, Lin BX, Yan CH (2004) J Phys Chem B 108:12481-12488
52. Hadjivanov KI, Vayssilov GN (2002) Adv Catal 47:307-511
53. Vivier L, Duprez D (2010) ChemSusChem 3:654-678
54. Vidruk R, Landau MV, Herskowitz M, Ezersky V, Goldbourt A (2011) J Catal 282:215-227
55. Binet C, Daturi M, Lavalley JC (1999) Catal Today 50:207-225
56. Conesa J (1995) Surf Sci 339:337-352

Figure captions

Fig. 1. Scheme of one-pot process for converting of valeric acid into nonane.

Fig. 2. XRD patterns of metal oxides unreduced and reduced by H_2 (a) ZrO_2 and (b) $10\%CeO_2/ZrO_2$, m - monoclinic phase, t - tetragonal phase of ZrO_2.

Fig. 3. HRTEM image and EDX spectrum of ZrO_2 particle of monoclinic phase attached to tetragonal ZrO_2 for $10\%CeO_2/ZrO_2$ oxide reduced by H_2. The corresponding Fourier image is inserted into the micrograph. Dark (red and black) arrows point to the intergrain boundary. White arrow points to lattice plane [110].

Fig. 4. HRTEM image and EDX spectrum of $10\%CeO_2/ZrO_2$ sample reduced by H_2. White arrow points to lattice plane [110]. Table inserted contains EDX elemental composition of ZrL and CeL in different regions of $10\%CeO_2/ZrO_2$ sample

Fig. 5. Zr3d XPS spectra of ZrO_2 and $10\%CeO_2/ZrO_2$ oxides unreduced and reduced by H_2.

Fig. 6. Ce3d XPS spectra of $10\%CeO_2/ZrO_2$ oxides unreduced and reduced by H_2.

Fig. 7. O1s XPS spectra of ZrO_2 and $10\%CeO_2/ZrO_2$ oxides unreduced and reduced by H_2.

Fig. 8. UV-*vis* spectra of metal oxides unreduced and reduced by H_2 (a) ZrO_2, (b) CeO_2 and (c) $10\%CeO_2/ZrO_2$

Fig. 9. IR spectra of CO adsorbed on ZrO_2 and $10\%CeO_2/ZrO_2$ oxides reduced by H_2.

Fig. 10. Catalytic properties of Ce and Zr metal oxides in the ketonization of valeric acid in hydrogen. Reaction conditions: 628 K, 1 bar, H_2 flow rate 30 cm^3/min, valeric acid LHSV = $0.34 cm^3/(g \bullet h)$

Table 1. The structural parameters of ZrO_2 and 10%CeO_2/ZrO_2 unreduced and reduced by H_2

Sample	**Phase**	**Phase composition,%**	**D_{CSD}, nm**	**Lattice parameter, Å**
ZrO_2	monoclinic	51	10	a=5.14(1) b=5.19(1) c=5.32(1) ∠β=99.16°
	tetragonal	49	17	a=5.114(2)
ZrO_2 (H_2)	monoclinic	55	10	a=5.14(1) b=5.20(1) c=5.34(1) ∠β=99.21°
	tetragonal	45	17	a=5.111(2)
10%CeO_2/ZrO_2	monoclinic	6	-	-
	tetragonal	94	14	a=5.138(2)
10%CeO_2/ZrO_2 (H_2)	monoclinic	6	-	-
	tetragonal	94	14	a=5.134(2)

Table 2. Surface composition of ZrO_2 and 10%CeO_2/ZrO_2 unreduced and reduced by H_2 according to XPS data

Sample	**Surface composition, atomic %**					
	Zr^{4+}	**Ce^{3+}**	**Ce^{4+}**	**O^{2-}**		
ZrO_2	28.4	-	-	71.6		
				O′(55.57)	O″(12.30)	O‴(3.73)
ZrO_2 (H_2)	30.1	-	-	69.9		
				O′(58.02)	O″(9.12)	O‴(2.76)
10%CeO_2/ZrO_2	27.0	2.6	1.7	68.7		
				O′(53.58)	O″(11.54)	O‴(3.58)
10%CeO_2/ZrO_2 (H_2)	27.8	3.2	1.4	67.6		
				O′(54.69)	O″(8.23)	O‴(4.78)

O′-O(530.3 eV), O″-O(532.1 eV), O‴-O(528.6 eV)

Table 3. The absorption maxima attribution for ZrO_2 and 10%CeO_2/ZrO_2 UV-*vis* spectra

Sample	**Band, nm**	**Transition**	**Ref.**
CeO_2	236 280 334	$O \rightarrow Ce^{3+}$ $O \rightarrow Ce^{4+}$ Interband transition of CeO_2 (Ce^{n+}-O-Ce^{n+}, n=3, 4)	[46,47,49,51]
CeO_2 (H_2)	215 280 334 500-800	$O \rightarrow Ce^{3+}$ $O \rightarrow Ce^{4+}$ Interband transition of Ce_xO_2 (Ce^{n+}-O-Ce^{n+}, n=3, 4)	
ZrO_2	226, 265	$O \rightarrow Zr^{4+}$	[45,46,49]
ZrO_2 (H_2)	265	$O \rightarrow Zr^{4+}$	
10%CeO_2/ZrO_2	250, 270 270 306, 350, 380	$O \rightarrow Ce^{3+}$ $O \rightarrow Ce^{4+}$, $O \rightarrow Zr^{4+}$ Interband transitions of CeO_2 (Ce^{n+}-O-Ce^{n+}, Ce^{n+} -O- Zr^{4+}, n=3, 4)	[46-51]
10%CeO_2/ZrO_2 (H_2)	270 310 320-500 500-800	$O \rightarrow Ce^{3+}$, $O \rightarrow Ce^{4+}$, $O \rightarrow Zr^{4+}$ Interband transitions of CeO_2 (Ce^{n+}-O-Ce^{n+}, Ce^{n+} -O- Zr^{n+}, n=3, 4) Interband transitions of CeO_2 (Ce^{n+}-O-Ce^{n+}, Ce^{n+} -O- Zr^{n+}, n=3, 4) and Zr^{3+}d-d transition	

Table 4. Catalytic properties of CeO_2, ZrO_2 and 10%CeO_2/ZrO_2 oxides in the ketonization of valeric acid in hydrogen and nitrogen. Reaction conditions: 628 K, 1 bar, H_2 flow rate 30 cm^3/min, valeric acid LHSV = 0.34cm^3/(g•h)

Sample	**Conversion, %**		**Selectivity, %**		**S, m^2/g**
	H_2	N_2	H_2	N_2	
CeO_2	40	31	76	80	25
ZrO_2	83	66	78	80	105
10%CeO_2/ZrO_2	93	82	79	81	79

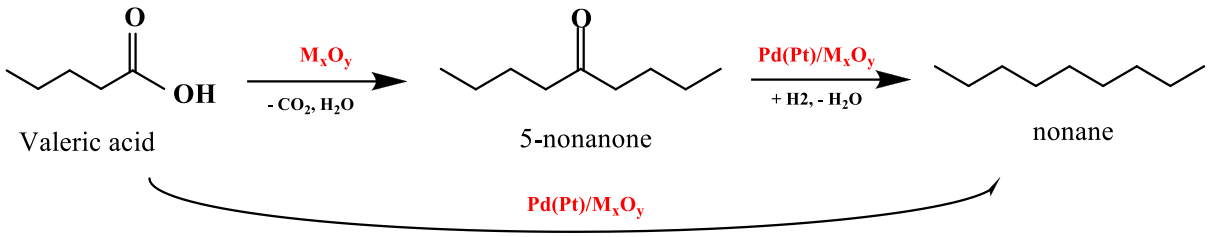

Fig. 1. Scheme of one-pot process for converting of valeric acid into nonane

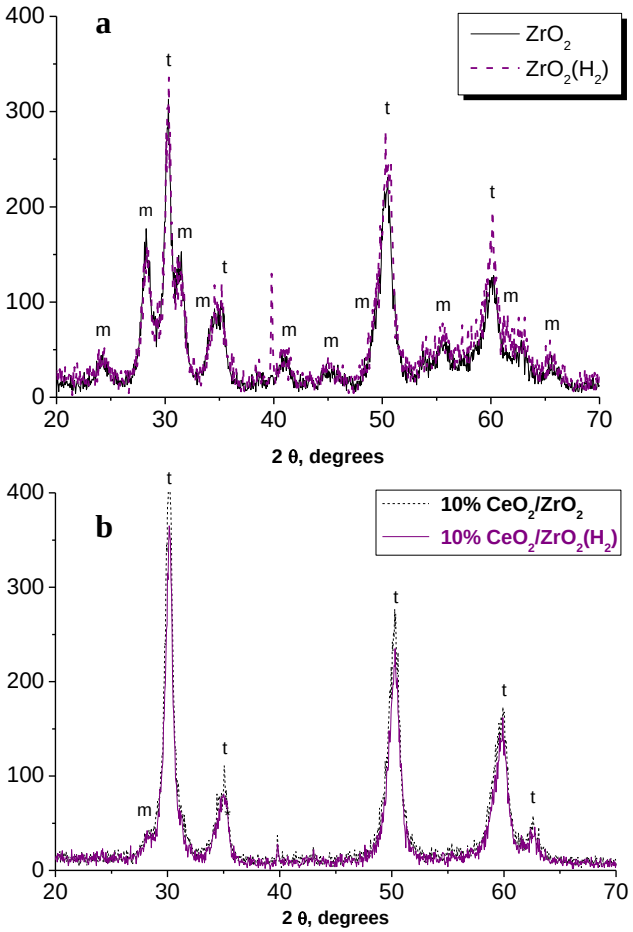

Fig. 2. XRD patterns of metal oxides unreduced and reduced by H_2 (a) ZrO_2 and (b) 10%CeO_2/ZrO_2, m - monoclinic phase, t - tetragonal phase of ZrO_2

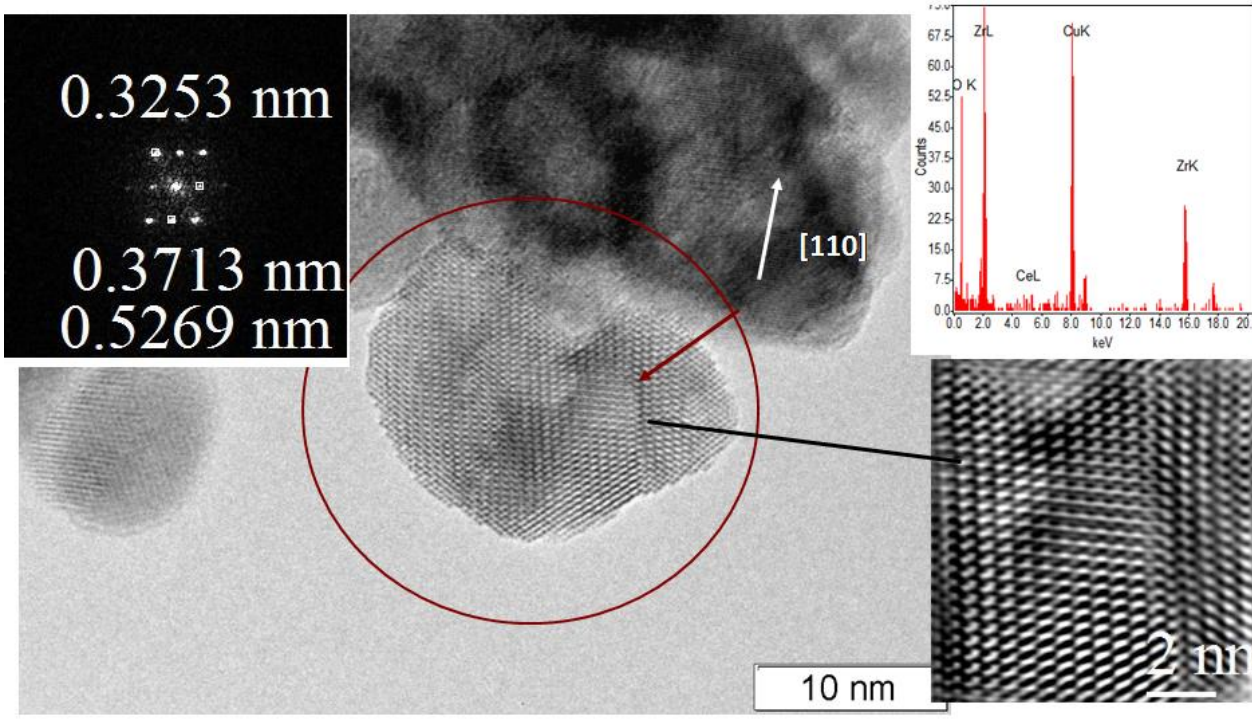

Fig. 3. HRTEM image and EDX spectrum of ZrO_2 particle of monoclinic phase attached to tetragonal ZrO_2 for 10%CeO_2/ZrO_2 oxide reduced by H_2. The corresponding Fourier image is inserted into the micrograph. Dark (red and black) arrows point to the intergrain boundary. White arrow points to lattice plane [110]

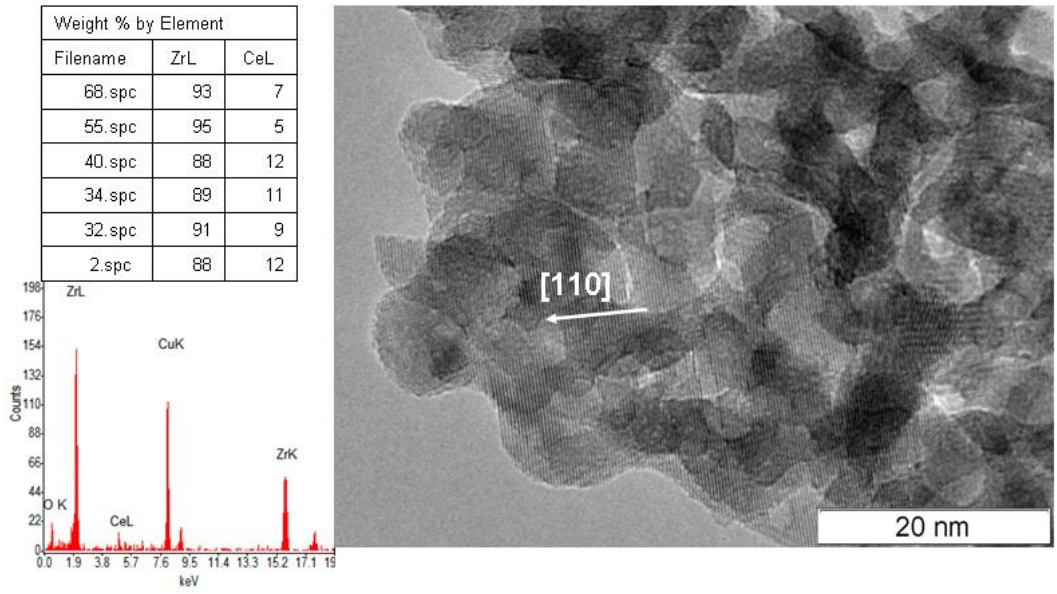

Fig. 4. HRTEM image and EDX spectrum of 10%CeO_2/ZrO_2 sample reduced by H_2. White arrow points to lattice plane [110]. Table inserted contains EDX elemental composition of ZrL and CeL in different regions of 10%CeO_2/ZrO_2 sample

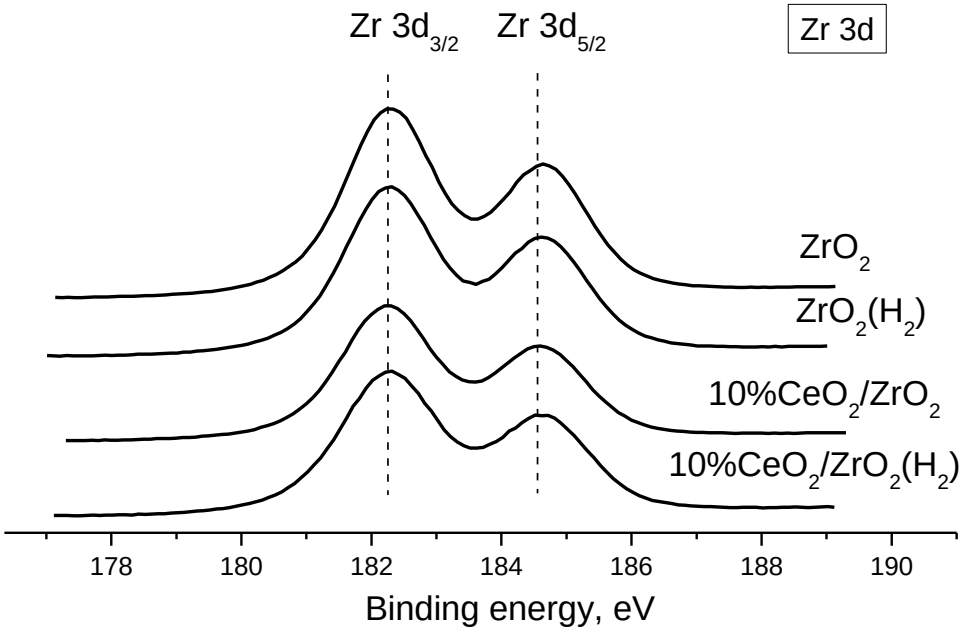

Fig. 5. Zr3d XPS spectra of ZrO_2 and 10%CeO_2/ZrO_2 oxides unreduced and reduced by H_2

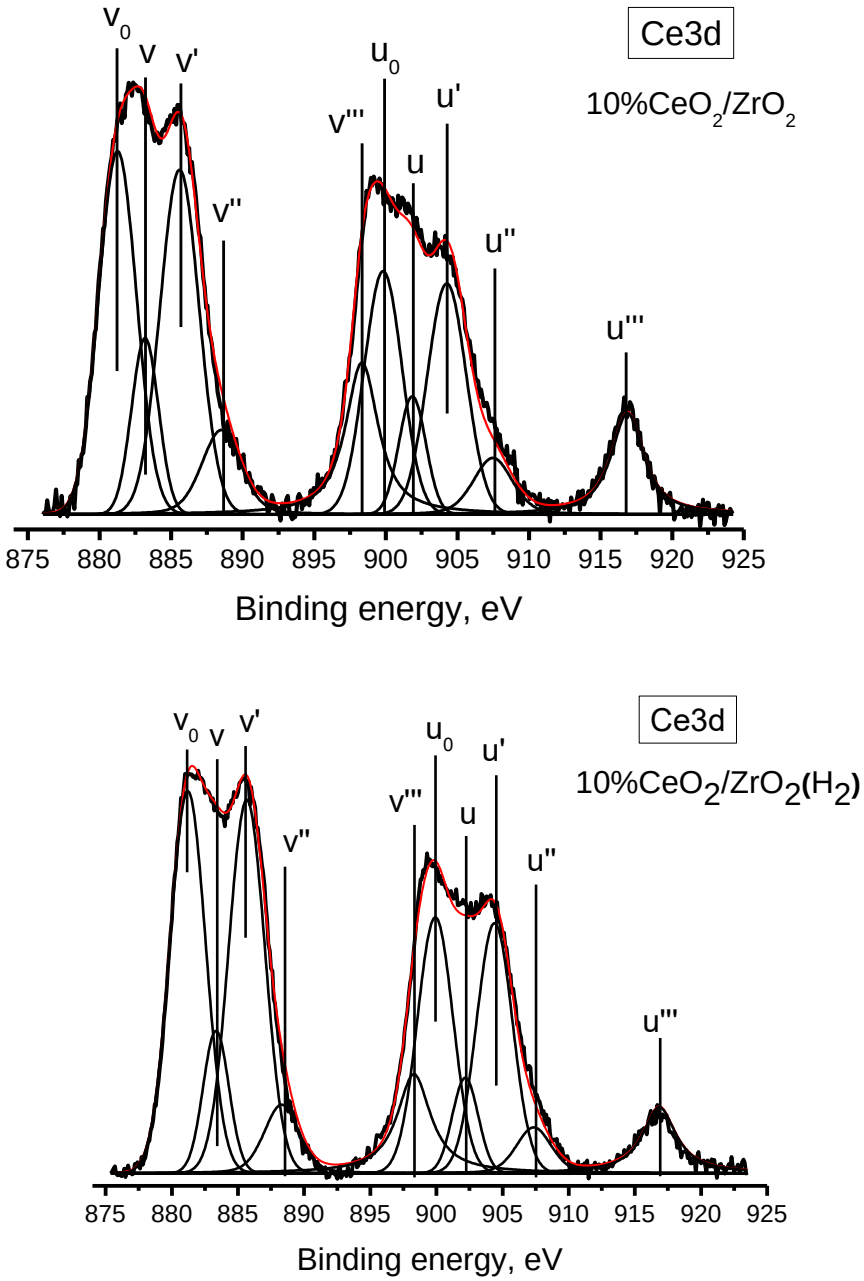

Fig. 6. Ce3d XPS spectra of 10%CeO_2/ZrO_2 oxides unreduced and reduced by H_2

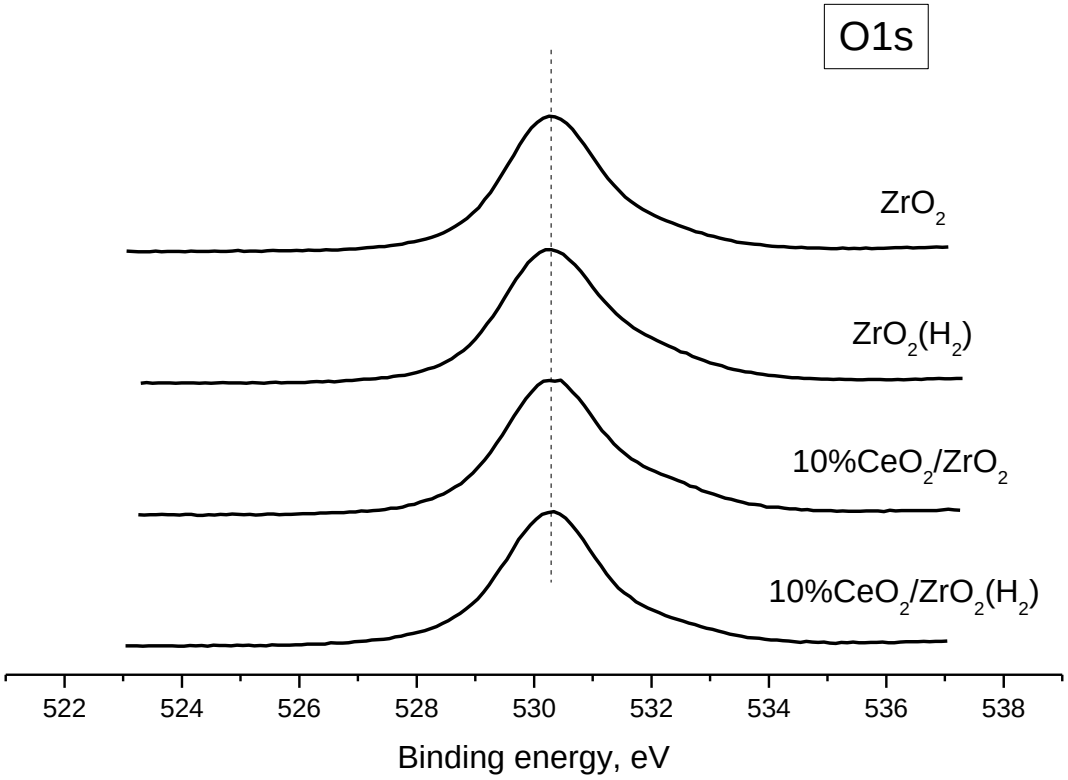
O1s
ZrO2
ZrO2(H2)
10%CeO2/ZrO2
10%CeO2/ZrO2(H2)
522
524
526
528
530
532
534
536
538
Binding energy, eV

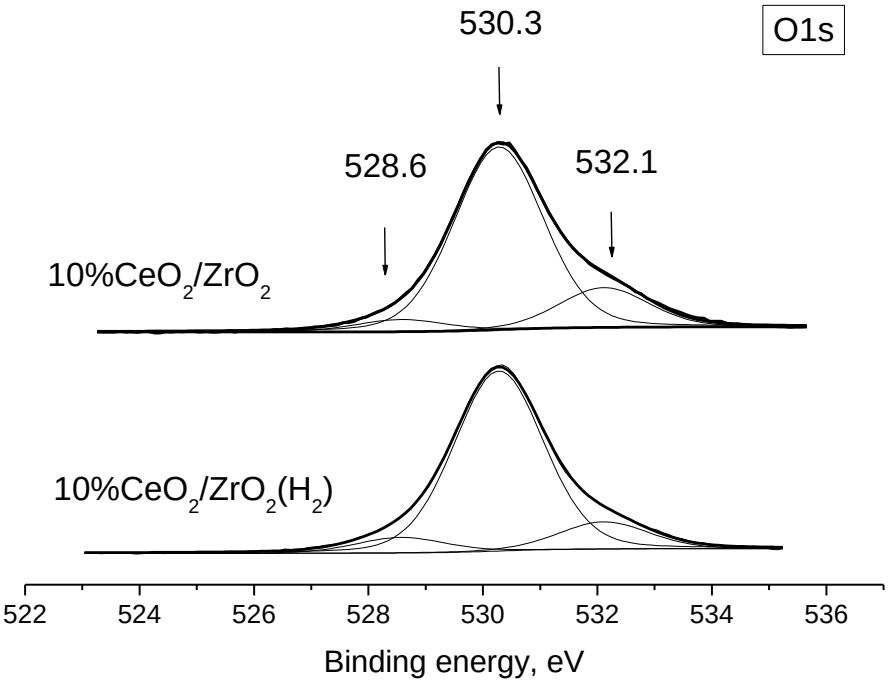
530.3
O1s
528.6
532.1
10%CeO2/ZrO2
10%CeO2/ZrO2(H2)
522
524
526
528
530
532
534
536
Binding energy, eV

Fig. 7. O1s XPS spectra of ZrO_2 and $10\%CeO_2/ZrO_2$ oxides unreduced and reduced by H_2

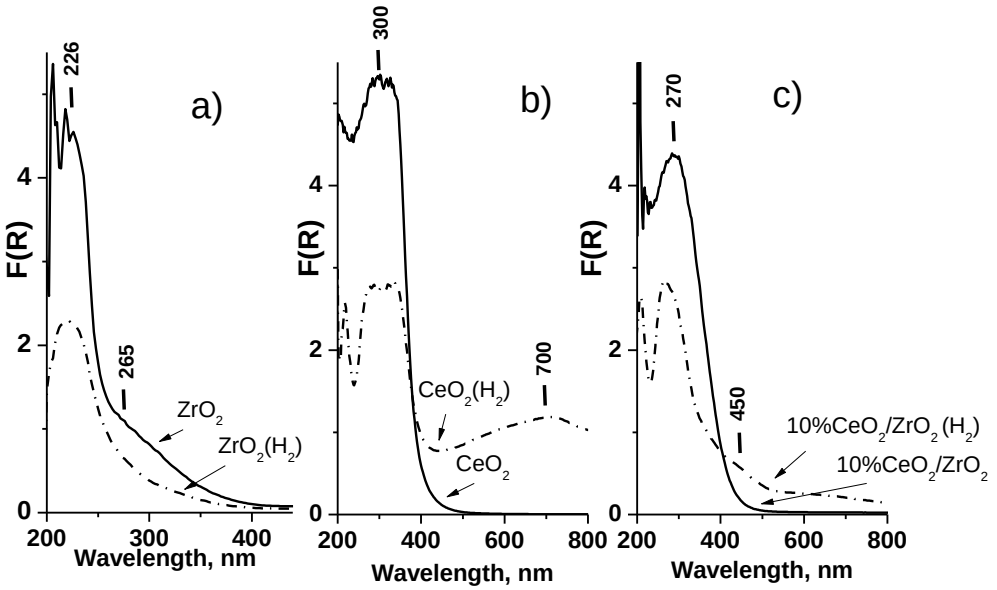

Fig. 8. UV-*vis* spectra of metal oxides unreduced and reduced by H_2 (a) ZrO_2, (b) CeO_2 and (c) $10\%CeO_2/ZrO_2$

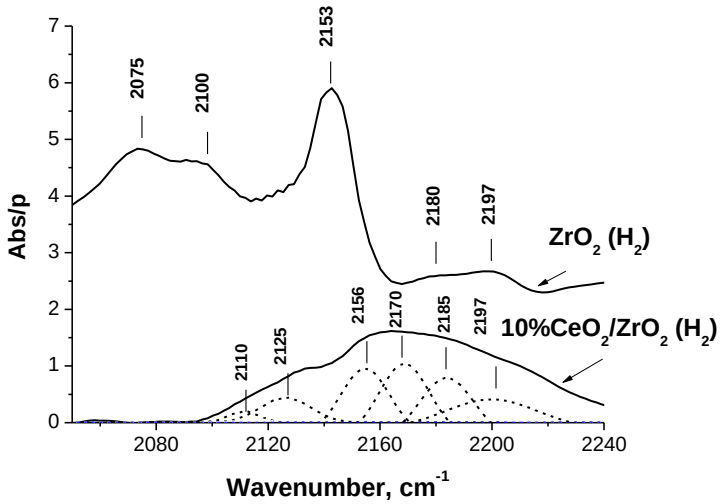

Fig. 9. IR spectra of CO adsorbed on ZrO_2 and 10%CeO_2/ZrO_2 oxides reduced by H_2

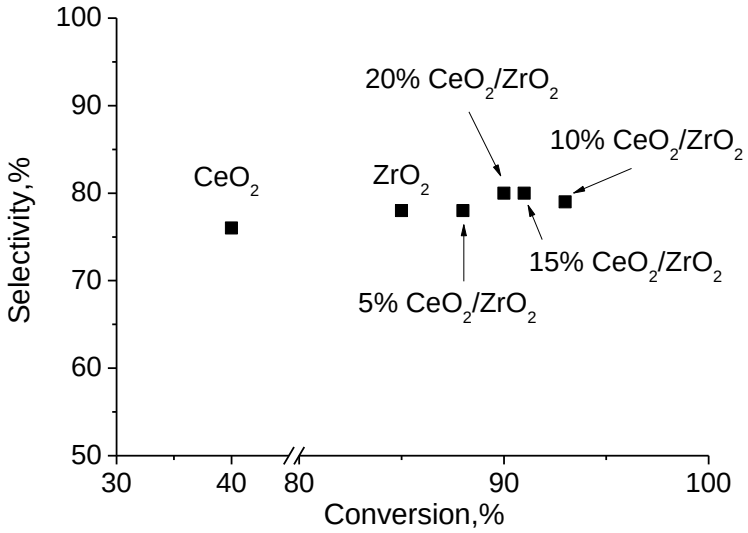

Fig. 10. Catalytic properties of Ce and Zr metal oxides in the ketonization of valeric acid in hydrogen. Reaction conditions: 628 K, 1 bar, H_2 flow rate 30 cm^3/min, valeric acid LHSV = 0.34cm^3/(g•h)